Controlling the Surface Energetics and Kinetics of Low-Bias Hematite for Solar Water Splitting Through Few Atomic Layers of NiO$_x$

Francesco Malara, Filippo Fabbri, Marcello Marelli, and Alberto Naldoni*

Dr. F. Malara, Dr. M. Marelli, Dr. A. Naldoni

CNR-Istituto di Scienze e Tecnologie Molecolari

Via Golgi 19, 20133 Milan, Italy

Email: a.naldoni@istm.cnr.it

Dr. F. Fabbri

IMEM-CNR

Parco Area delle Scienze 37/A, 43100 Parma, Italy

Abstract

Photoanodes for photoelectrochemical water splitting require the use of a large applied potential to sustain high photocurrent. This has been conventionally addressed by depositing electrocatalysts on semiconductors to boost the kinetics of water oxidation. Herein, it is shown that the advance in the onset potential (V_{ON}) of hematite (α-Fe$_2$O$_3$) is regulated not by the activity of the overlayer, but rather by how it modifies the surface properties of the electrode. NiO$_x$ catalysts induce different and opposite effects on the *J-V* curve of α-Fe$_2$O$_3$ when deposited with different methodologies. Electrodeposited NiO$_x$ produces only an increase of photocurrent at high bias, while photodeposited NiO$_x$ induces also a 200 mV cathodic shift of V_{ON}, which reaches 0.58 V. Cathodoluminescence spectroscopy and open circuit potential decay reveal that only through photodeposition a complete passivation of surface defects is achieved. This produces a decrease of electron-hole recombination and a substantial shift of the quasi-Fermi level in light. At the same time, the Fermi level in dark reaches a new energetic level. Electrochemical impedance spectroscopy on NiO$_x$ photodeposited shows a 4 times reduction of charge transfer resistance accounting for the low V_{ON}. This study shows that surface energetics and kinetics of photoanodes are tightly connected. Only though a complete control of the former it is possible to achieve new performing interfaces for low-bias water splitting.

1. Introduction

Hematite (α-Fe$_2$O$_3$) is one of the most promising anode materials for photoelectrochemical (PEC) water splitting due to its energy gap (2.1 eV), excellent chemical stability, and earth abundance.[1–3] However, the performance of α-Fe$_2$O$_3$ has been limited by the low electron mobility (10^{-2} cm^2 V^{-1} s^{-1}) and the short hole diffusion length (5 nm),[4] which decrease the charge separation efficiency. Doping with M^{4+} elements (e.g., Si, Ti, Sn) and growth of nanostructures such as cauliflowers,[1] nanowires,[5–7] nanorods,[4] nanotubes,[8] and hierarchical platelets[9] have been used to overcome these restrictions by increasing carrier densities, interfacial area and decreasing the distances that

2

minority carriers have to travel to reach the electrode/electrolyte interface.[4,10,11] Despite this amelioration, most of α-Fe$_2$O$_3$ photoelectrodes show an onset potential (V_{ON}) of 1.0 V *vs.* RHE (reversible hydrogen electrode). The recalcitrant electron-hole recombination is dependent on interface phenomenas and hinders the generation of significant photocurrent at low bias, a crucial point when considering a tandem cell approach.[12,13]

It is possible to distinguish two main interfaces in α-Fe$_2$O$_3$ electrodes for PEC water splitting: (i) the FTO/α-Fe$_2$O$_3$ interface, and (ii) the α-Fe$_2$O$_3$/electrolyte interface. It has been shown that depositing an underlayer of SiO$_x$,[14] Nb$_2$O$_5$, or Ga$_2$O$_3$[11,15] suppresses the back electron injection into the electrolyte from uncovered FTO, inducing up to a 100-150 mV V_{ON} advancement. Otherwise, the electrode/electrolyte interface has been typically modified with the deposition of an electrocatalyst such as Co-Pi,[16,17] FeOOH,[18] NiOOH,[19] and IrO$_2$[9,20] as well as inactive overlayers such as Al$_2$O$_3$, Ga$_2$O$_3$ and In$_2$O$_3$ to achieve the shifting of V_{ON} to more negative potentials.[10,11,21] This improvement in V_{ON} is a key aspect to enable unassisted water splitting using tandem configurations[12] and therefore it is crucial to understand its nature. The role of overlayers for α-Fe$_2$O$_3$ photoanodes has been extensively debated[3,10,22–24] and it was recently suggested that the observed V_{ON} cathodic shift is related to surface state passivation rather than to surface catalysis.[10,12,24] However, the understanding on the definitive role of overlayers in changing α-Fe$_2$O$_3$ surface properties and PEC performance in terms of V_{ON} remain elusive.

Herein we use one of the most efficient electrocatalysts for oxygen evolution, i.e. NiO$_x$,[18,19,25–28] as overlayer on α-Fe$_2$O$_3$ to show why its surface modification produces a cathodic shift in V_{ON} of PEC water splitting. Through electrodeposition and photodeposition we cover the α-Fe$_2$O$_3$ surface with few atomic layers of amorphous NiO$_x$. Although the chemical composition of both deposits is similar, the two NiO$_x$ overlayers have profoundly different effect on the photocurrent vs. potential curve of our photoanodes. NiO$_x$ electrodeposited shows the same V_{ON} of bare α-Fe$_2$O$_3$ and an increased photocurrent density only at $E > 0.8$ V$_{RHE}$. On the other hand, NiO$_x$ photodeposited is able to advance V_{ON} of about 200 mV. Only this treatment decreases the electron-hole recombination due

to bandgap excitation through a complete passivation of surface defects as seen by cathodoluminescence spectroscopy. This shifts the quasi-Fermi in light of 110 mV to more positive energy (0.5 V_{RHE}), a value close to the flat band potential (0.48 V_{RHE}). The change in surface energetics in α-Fe$_2$O$_3$/NiO$_x$ photodeposited is responsible for the creation of a novel interface that exchanges charges with water four times faster than α-Fe$_2$O$_3$ and α-Fe$_2$O$_3$/NiO$_x$ electrodeposited. These results highlight how surface energetics regulates the kinetics and PEC performance of low-bias α-Fe$_2$O$_3$ photoanodes for solar water splitting.

2. Results and Discussions

Figure 1 shows the cyclic voltammetry (CV) in light of bare α-Fe$_2$O$_3$ and the best NiO$_x$ electro- and photodeposited coated α-Fe$_2$O$_3$ photoanodes. Both deposition treatments produce an enhancement of water oxidation efficiency. α-Fe$_2$O$_3$/NiO$_x$ electrodeposited shows high increase of the J curve slope between $0.8 \text{ V} < E < 1 \text{ V}$ (all potentials are referred *vs.* RHE) and a general increase of the photocurrent with respect to α-Fe$_2$O$_3$ at $E > 0.8$ V. This behaviour, perhaps more similar to the effect produced by the nanostructuring of the semiconductor, differs from the reduction of the overpotential expected after the application of a catalyst, which should primarily generate an advancement of the onset potential (V_{ON}).[20] Differently, the NiO$_x$ photodeposition method induces both an increase of photocurrent (more than 40% at 1.23 V vs. RHE) and a cathodic shift of V_{ON}. V_{ON} of α-Fe$_2$O$_3$/NiO$_x$ photodeposited is 0.58-0.6 V, 200 mV more cathodic than bare α-Fe$_2$O$_3$ ($V_{ON} = 0.8$ V)[22] and α-Fe$_2$O$_3$/NiO$_x$ electrodeposited electrodes.

To further confirm this trend, we report in Figure S2 and S3 the J-V curves for α-Fe$_2$O$_3$/NiO$_x$ electro- and photodeposited obtained at different deposition time, respectively. It is evident that the electrodeposition produces only a gradual photocurrent increase at increasing the deposition time, while for NiO$_x$ photodeposition we observe a monotonic advance of the V_{ON} and a higher plateau photocurrent too.

In principle, NiO$_x$ deposits generated through either electrodeposition or photodeposition are similar in composition and nature, as for that a similar electrocatalytic activity is expected. Therefore, the reasons underlying the different *J-V* curve for α-Fe$_2$O$_3$/NiO$_x$ electrodeposited and α-Fe$_2$O$_3$/NiO$_x$ photodeposited might be due different NiO$_x$ morphology and/or on the different junctions formed at the α-Fe$_2$O$_3$ surface and how their properties influence water oxidation.

In order to fully unravel the reasons that produce the cathodic shift of onset potential when an overlayer (i.e., NiO$_x$) is applied to a semiconductor (i.e., α-Fe$_2$O$_3$), we conduct a deep morphological, structural, physicochemical, and electrochemical characterization of the α-Fe$_2$O$_3$, α-Fe$_2$O$_3$/NiO$_x$ electrodeposited, and α-Fe$_2$O$_3$/NiO$_x$ photodeposited photoanodes.
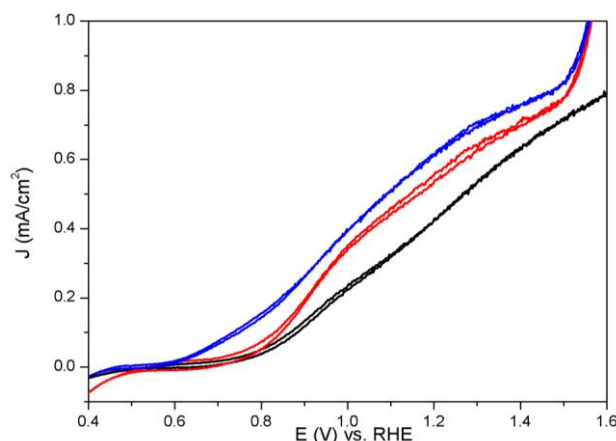
Figure 1. PEC activity of bare α-Fe$_2$O$_3$ (black line), α-Fe$_2$O$_3$/NiOx electrodeposited for 1800 s (red line), and α-Fe$_2$O$_3$/NiOx photodeposited for 600 s electrodes (blue line).

SEM and TEM analysis (**Figure 2**) reveal the coral-like structure of our α-Fe$_2$O$_3$ films, which are based on interconnected crystalline globular grains of 75-100 nm in width. From XRD pattern (Figure S1 in the Supporting Information) the (110) and the (300) reflections belonging to α-Fe$_2$O$_3$ (R$\overline{3}$c H setting) are clearly visible. The complete extinction of (hkl) peaks with l ≠ 0 indicates a strong orientation of (001) crystallographic planes orthogonally to the FTO surface.[9,19]

Figures 2a and 2b show SEM top view images of the superficial morphology of α-Fe$_2$O$_3$ after sintering. From the cross sectional view of the electrode (Figure 2c) it is possible to distinguish the different layers forming the scaffold of our photoanodes: α-Fe$_2$O$_3$ (~250 nm), FTO and glass.

TEM images highlight that either through electrodeposition (Figure 2d and 2e) or photodeposition (Figure 2f and 2g) we cover α-Fe_2O_3 photoanodes with an amorphous thin layer of NiO_x. High resolution TEM highlights 2 nm (Figure 2e) and 1 nm (Figure 2g) thick NiO_x layers obtained by using electrodeposition and photodeposition, respectively.

In order to better characterize the thickness and distribution of NiO_x we use Electron Spectroscopic Imaging (ESI) analysis. ESI maps show the co-presence of Fe and Ni in both the α-Fe_2O_3/NiO_x electrodes. Fe distribution is homogeneous for both samples, while the elemental Ni distribution varies when considering electrodeposited (Figure 2h) and photodeposited NiO_x (Figure 2i). Strikingly, comparing the ESI maps of Ni at higher magnification we observe a much more homogeneous and smoother layer/signal for the photodeposited NiO_x (Figure 2m) with respect to the electrodeposited one (Figures 2l), that results more uneven. The latter presents areas where the Ni result more concentrated, reaching 6-7 nm thickness. The photodeposited NiO_x thickness is more regular and about 1 nm. NiO_x layer appears to preferentially accumulate onto the grain surface as enhanced Ni signals on the grains border are detected (especially for NiO_x electrodeposited, see Figure 2l).

The chemical composition of the NiO_x deposited on the α-Fe_2O_3 surface by using electro- and photodeposition can play an important role in finding correlations with PEC activity. **Figure 3**a reports the CV measurements in the dark of bare α-Fe_2O_3 (black line), α-Fe_2O_3/NiO_x electrodeposited (red line), and α-Fe_2O_3/NiO_x photodeposited (blue line) electrodes. α-Fe_2O_3/NiO_x electrodeposited show only one peak at lower potential (1.25 V) that represents the oxidation from Ni^{2+} to Ni^{3+} for the Ni hydroxide (α phase) to Ni-oxyhydroxide (γ phase) transition.[27,29] the case of photodeposited NiO_x, the layer has a mixed composition of $\alpha/\beta-NiO_x$, with the β-phase being the prevailing one (Figure 3a).

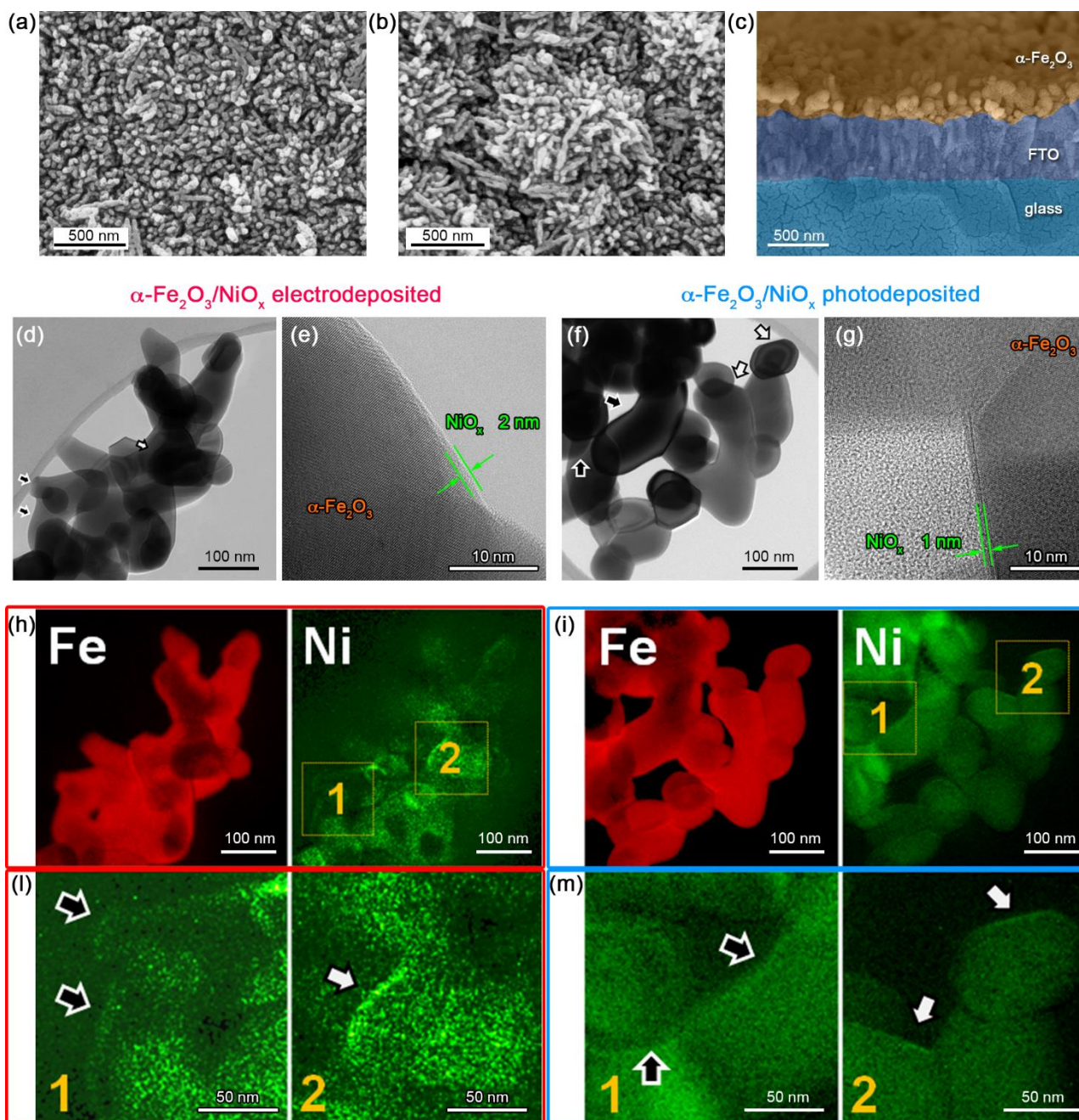**Figure 2.** a,b) Top view and c) Cross-sectional SEM images of hematite electrode: α-Fe$_2$O$_3$, FTO and glass are highlighted by using different colours. d-g) TEM images at different magnification of α-Fe$_2$O$_3$/NiOx electrodeposited (d,e) and α-Fe$_2$O$_3$/NiOx photodeposited (f,g). The TEM micrographs highlight the thickness and morphology of NiO$_x$ overlayer. h-m) elemental distribution ESI map (Fe and Ni) of α-Fe$_2$O$_3$/NiOx electrodeposited (h,l) and α-Fe$_2$O$_3$/NiOx photodeposited (i,m) electrodes.

XPS survey spectra for both α-Fe$_2$O$_3$/NiO$_x$ electrodeposited and photodeposited show Fe and Ni signals along with those from elements that constitute the FTO substrate (Figure 3a and S4). α-Fe$_2$O$_3$/NiO$_x$ electrodeposited contains the 3 at.% of Ni, while the NiO$_x$ photodeposited a 0.6 at.% of

Ni. This confirms that with electrodeposition a higher amount of NiO_x covers the top of the α-Fe_2O_3 surface. The Fe 2p XPS spectra (Figure 3b) presented the typical shape of α-Fe_2O_3 samples.[6] We perform high-resolution scan on the Ni binding energy (BE) region to investigate the species forming the electrodeposited NiO_x layer (Figure 3c). Ni 2p spectrum shows a complex structure with intense shake-up peaks (satellite) at higher BE (861.9 and 879.2 eV) adjacent to the main peaks, i.e. $2p_{3/2}$ 855.4 and $2p_{1/2}$ 872.9 eV. The Ni $2p_{3/2}$ can be deconvoluted into two peaks located at 855.3 and 857.8 eV, which are consistent with the presence of Ni^{2+} and Ni^{3+} ($Ni^{3+}/Ni^{2+} \sim 0.4$), respectively.[30] The low atomic % of Ni at the surface of the photodeposited sample hinders the chance to perform Ni high resolution analysis. Nevertheless, we are confident that through α-Fe_2O_3 bandgap excitation we generate holes with enough energy to oxidize Ni^{2+} to Ni^{3+}.[16] Analysis of the oxygen peaks of bare α-Fe_2O_3, α-Fe_2O_3/NiO_x electrodeposited and photodeposited (Figure 3c,d,e respectively) show the presence of three components, attributed to lattice oxygen ($O_{lattice}$), surface OH (O_{OH}) species, and surface adsorbed water (O_{H_2O}) molecules.[31] Table S1 reports the BE of oxygen species and relative atomic % ratio for all samples investigated. The O_{OH} / $O_{lattice}$ ratio increased when considering the α-Fe_2O_3/NiO_x samples with respect to bare α-Fe_2O_3. In addition, it is interesting to note that O_{H_2O} / $O_{lattice}$ ratio is only slightly increased passing from α-Fe_2O_3 to α-Fe_2O_3/NiO_x electrodeposited. The electrodeposited NiO_x do not cover homogeneously (see TEM images, Figure 2) the α-Fe_2O_3 surface and the XPS signal is therefore averaged between the two contributions. Otherwise, O_{H_2O} / $O_{lattice}$ decreases by 30 % when the NiO_x is photodeposited since the β/β phaseis the dehydrated NiO_x phase and mainly forms the overlayer. As reported by Bode et al,[29] the different configurations imply different atomic packing, in particular α/γ structure results more open and then more permeable to the water and to the ions, while β/β configuration is more compact.

The different composition of NiO_x overlayers can be understood considering the different experimental conditions of electrodeposition and photodeposition. By working at fixed potential during the electrodeposition, we control the NiO_x layer composition that is a mixture of α/γ NiO_x

phase with a Ni^{3+}/Ni^{2+} ratio of ~0.4. Moreover, the application of a constant potential induces a higher amount (and proportional to deposition time) of deposited NiO_x because a constant current flow is maintained trough the electrochemical cell.
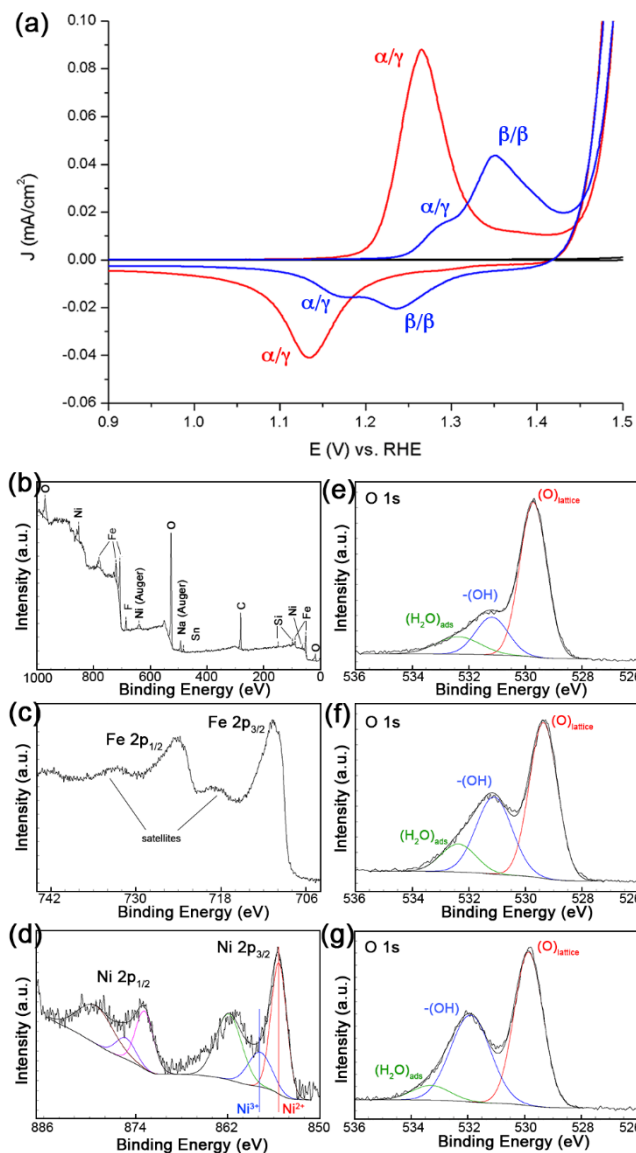

Figure 3. a) Cyclic voltammetry in dark of bare α-Fe_2O_3, α-Fe_2O_3/NiO_x electrodeposited (red line) and α-Fe_2O_3/NiO_x photodeposited (blue line). b) XPS survey spectrum of α-Fe_2O_3/NiO_x electrodeposited. c,d) High resolution XPS scan of Fe 2p and Ni 2p regions for the α-Fe_2O_3/NiO_x electrodeposited photoanode. e-g) High resolution XPS scan of O 1s region of pure α-Fe_2O_3 (e), α-Fe_2O_3/NiO_x electrodeposited (f) and α-Fe_2O_3/NiO_x photodeposited (g).

Conversely, the photodeposition produce a mixture of α/γ (a minor fraction) and β/β phase layer having Ni both in 2+ and 3+ oxidation states.[27,28] By working in light under open circuit conditions, the net current flow is zero and this produces an ultrathin film of about 1 nm thickness (similar for all

deposition times), which would corresponds roughly to three stacked atomic layers of β−NiOOH. In this case all the surface sites are activated by the solar irradiation and this enable the growth of a homogeneous and smooth NiO_x overlayer.

NiO$_x$ composition has been reported to be important for electrochemical water oxidations activity where the β−NiOOH was reported to be more active than the α/γ−NiOOH.[26,29] Since both the phases of NiOOH are good electrocatalysts we would expect to see for both an advance in V_{ON}. As a matter of fact, we observe only this behaviour for α-Fe$_2$O$_3$/NiO$_x$ photodeposited systems. This bring us to hypothesize that when an electrocatalyst, i.e. NiO$_x$, is coupled to α-Fe$_2$O$_3$, V_{ON} mostly depends on the semiconductor properties and on how these are altered by the surface modification, rather than the electrocatalytic activity of the overlayer itself.[10,21,24,32]

The onset potential of the NiO$_x$-coated α-Fe$_2$O$_3$ electrodes may be regulated by different processes such as effective charge transfer across the α-Fe$_2$O$_3$ / NiO$_x$ / water interfaces, quenching of internal recombination and passivation of surface defects.

We analyze both the physicochemical and electrochemical properties of α-Fe$_2$O$_3$/NiO$_x$ photoanodes to find a plausible explanation of the onset potential shift seen for NiO$_x$ photodeposited sample with respect to bare α-Fe$_2$O$_3$ and the NiO$_x$ electrodeposited one.

To gain direct insights on how the NiO$_x$ deposition affects charge recombination within α-Fe$_2$O$_3$, we carried out cathodoluminescence (CL) spectroscopic measurements.

The CL spectrum of pristine α-Fe$_2$O$_3$ (**Figure 4**, black line) shows a complex emission due to four main different components set at 3.17 eV, 2.76 eV, 2.45 eV and 2.18 eV (see deconvolution in Figure S5).[33] The emission at 2.18 eV and 2.45 are mainly related to the double exciton process.[34] Light emissions at energies higher than the optical bandgap were previously reported in α-Fe$_2$O$_3$ spindle-shaped nanoparticles[35] and one-dimensional α-Fe$_2$O$_3$ nanostructures.[33] The light emission bands centred at about 3.17 eV, and 2.76 eV are not attributed to quantum confinement effects but rather to ligand to metal charge transfer (LMCT) transitions.[35]
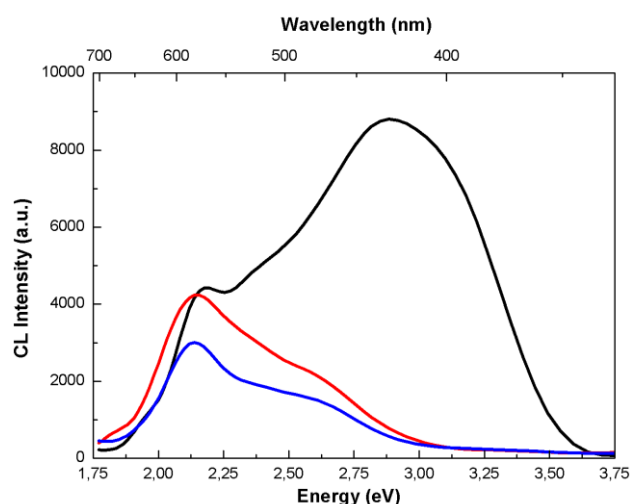
10

Figure 4. Cathodoluminescence (CL) spectra of α-Fe$_2$O$_3$ (black curve), α-Fe$_2$O$_3$/NiOx electrodeposited (red curve), and α-Fe$_2$O$_3$/NiOx photodeposited (blue curve).

After NiO$_x$ deposition, either via electrodeposition (red line) or photodeposition (blue line), we observe a complete quenching of the CL signal due to electron-hole recombination corresponding to LMCT transitions. For the best of our knowledge, this quenching was not previously reported for α-Fe$_2$O$_3$. A similar effect was reported in the case of europium doped yttrium oxide nanoparticles passivated with acetylacetonate.[36] In that case the LMCT transition was related to the charge transfer from oxygen vacancies to europium dopant. Various studies on nanocrystalline α-Fe$_2$O$_3$ particles have confirmed that photoluminescence relative to direct hole-electron recombination is highly dependent on surface quality and, especially, on surface trap density.[35, 36] Therefore we can hypothesize that the 3.17 eV and the 2.76 eV emissions can be related to the LMCT transition from hematite surface defects, as oxygen vacancies, to iron atoms.

The inhibition of recombination due to LMCT transitions after NiO$_x$ deposition (i.e., due to oxygen vacancies passivation by hydroxyl-groups in NiO$_x$) might be correlated to higher photocurrent density seen for both α-Fe$_2$O$_3$/NiO$_x$ electrodeposited and photodeposited. Nevertheless, the discussed quenching cannot be responsible for the shift of onset potentials observed for the different electrodes.

Importantly, α-Fe$_2$O$_3$ optical bandgap emission intensity (i.e., component at 2.19 eV) decreases only in the case of NiO$_x$ deposited with the photo-assisted process (Figure 4). This suggests

11

a direct correlation between electron-hole recombination due to bandgap excitation and the onset potential of our photoanodes. Only the photodeposition of NiO_x produces an effective quenching of charge recombination thus inducing a cathodic shift of V_{ON} for α-Fe_2O_3/NiO_x photodeposited.

The behaviour of photoanodes can be modelled in terms of Schottky diode junction formed at the electrode/electrolyte interface.[24,37] The anodic photocurrent is controlled by the quality of the junction and the charge transfer across the solid/liquid interface, as described in equation *(1)* and *(2)*:

$$\frac{P_S}{P_S^0} = \exp\left(-\frac{q\Phi}{kT}\right) = \exp\left[-\frac{q\left(E + V_{ph} - V_{CB}\right)}{kT}\right] \tag{1}$$

$$i_p = i_p^0 \left\{ \frac{P_S}{P_S^0} \exp\left(\frac{q\alpha_p\eta}{kT}\right) - \exp\left[-\frac{q\left(1-\alpha_p\right)\eta}{kT}\right] \right\} \tag{2}$$

Where, P_s is the surface hole concentration, P_s^0 is the equilibrium surface hole concentration, q is the charge of electrons, Φ is the magnitude of the band bending as defined by the difference between the combination of applied potential (E) and photovoltage (V_{ph}, defined as the difference in the Fermi levels between dark and light) and the conduction band edge (V_{CB}), α_p is the hole transfer coefficient; η is the overpotential, which is the difference between the quasi-Fermi level of holes and the electrochemical potential of the solution, k is the Boltzmann constant, T is temperature, i_p^0 is the current in the dark, and i_p is the photocurrent in light.[24]

Both equations relate on the number of holes that reach the electrode/electrolyte interface and each of them can alter the *J-V* curve. Nonetheless, eq. *(1)* describes the dependence of surface holes concentration on purely energetic terms, whereas eq. *(2)* reports its dependence on the charge-transfer kinetics and thus overpotential needed to drive the water oxidation reaction.

In order to understand the underlying mechanism that induces the cathodic shift of V_{ON} only in α-Fe_2O_3/NiO_x photodeposited, we study separately the energetics and the kinetics of our photoanodes.

The energetics of photoanodes (eq. *(1)*) depends on band bending, and in turn on photovoltage. Surface states produce Fermi level pinning, which implies that the Fermi level and the band edge

positions at the surface appear to be fixed. As a result, the degree of surface band bending would not change when the applied potential is increased. Fermi level pinning has been shown to be an important reason for late V_{ON}.[24,38] We also expect that the presence of surface defects may move the Fermi level towards the energy positive direction.[24]

In order to gather information specific to surface energetics before and after NiO_x deposition, we probe the quasi-Fermi level of the semiconductor in light and dark conditions through open circuit voltage (V_{OC}) decay measurements. Because the measurements are conducted under zero steady-state current, influences by surface charge-transfer kinetic factors are excluded.[12,24]

Figure 5a shows three cycles (light on/light off) of V_{OC} analysis until a good stabilization of the photoanodes is obtained. Bare α-Fe_2O_3 (black line) presents a stable V_{OC} in light of ~0.61 V. If we consider dark conditions the energy level moves towards more positive values that, after each cycle, tend to 0.85 V. The plot of the α-Fe_2O_3/NiO_x electrodeposited electrode (red line) shows a quasi-Fermi level in light of 0.57 V. When the light is switched off, initially the V_{OC} falls at 0.88 V and subsequently rise up slowly, asymptotically approaching 0.85 V, i.e. the same V_{OC} of bare α-Fe_2O_3. Differently, the V_{OC} in light of α-Fe_2O_3/NiO_x photodeposited (blue line) is 0.5 V, the less positive value among our photoanodes. As the light is switched off the potential quickly falls down to 0.85 V and later grows up towards 0.75 V.

V_{OC} decay analysis gives also useful information about the recombination rate into PEC system: the faster the voltage decay observed, the higher is the recombination.

If the V_{OC} plots are reported in log scale (Figure 5b), it is possible to appreciate the different recombination mechanisms. The first part of decay is ascribable to internal recombination: a part of the exited electrons fall down to valence band and others move toward the intraband trapping sites. Both processes are really fast.[32,39] Subsequently, the slow potential decrease means that the charges locked into the trapping sites are released into the electrolyte. This decay is slower because diffusive processes control recombination events. In the case of the bare α-Fe_2O_3 these two processes are very well defined: from 0.61 V to 0.66 V the decay is very fast, after that the decay proceed slower. For

the α-Fe$_2$O$_3$/NiO$_x$ electrodeposited photoanode, the net change of behaviour disappears and this means that the decay process follows another way: not all the electrons of α-Fe$_2$O$_3$ are locked into trap sites, but a part of them starts to move toward the electrolyte through the NiO$_x$ overlayer. This implies a sort of continuity in the decay line. Moreover, it determines a faster decay process and the reaching of lower potential values. Anyway, after 400 s the potential of the electrode starts to increase again, stabilizing at about the same values observed for α-Fe$_2$O$_3$ (0.85 V). This means that α-Fe$_2$O$_3$ always controls the energetic levels between the electrode and the electrolyte since NiO$_x$ electrodeposition produces a discontinuous film (see Figure 2) and part of the α-Fe$_2$O$_3$ surface (and thus of surface defects) remains in contact with the electrolyte. In the case of the α-Fe$_2$O$_3$/NiO$_x$ photodeposited, the decay is similar to the electrodeposited one, but the Fermi level in dark reaches a new energetic equilibrium (0.75 V). The homogeneous and compact film of NiO$_x$ photodeposited prevents the contact between α-Fe$_2$O$_3$ and the electrolyte thus producing a new superficial energetic level characteristic of the ensemble α-Fe$_2$O$_3$-NiO$_x$.

Figure 5c summarizes the V_{OC} values found in light and dark condition for all the photoanodes analyzed. The quasi-Fermi levels measured in light conditions highlight a progressive shift toward less positive V_{OC} in the order α-Fe$_2$O$_3$ > α-Fe$_2$O$_3$/NiO$_x$ electrodeposited > α-Fe$_2$O$_3$/NiO$_x$ photodeposited. The electrodeposition of NiO$_x$ produces a V_{OC} (light) shift of 40 mV, while the NiO$_x$ photodeposition process is able to decrease the V_{OC} of bare α-Fe$_2$O$_3$ of 110 mV determining a V_{OC} = 0.5 V. The reason behind the drastic difference in V_{OC} observed for our photoanodes stands in the mechanism of NiO$_x$ deposition.
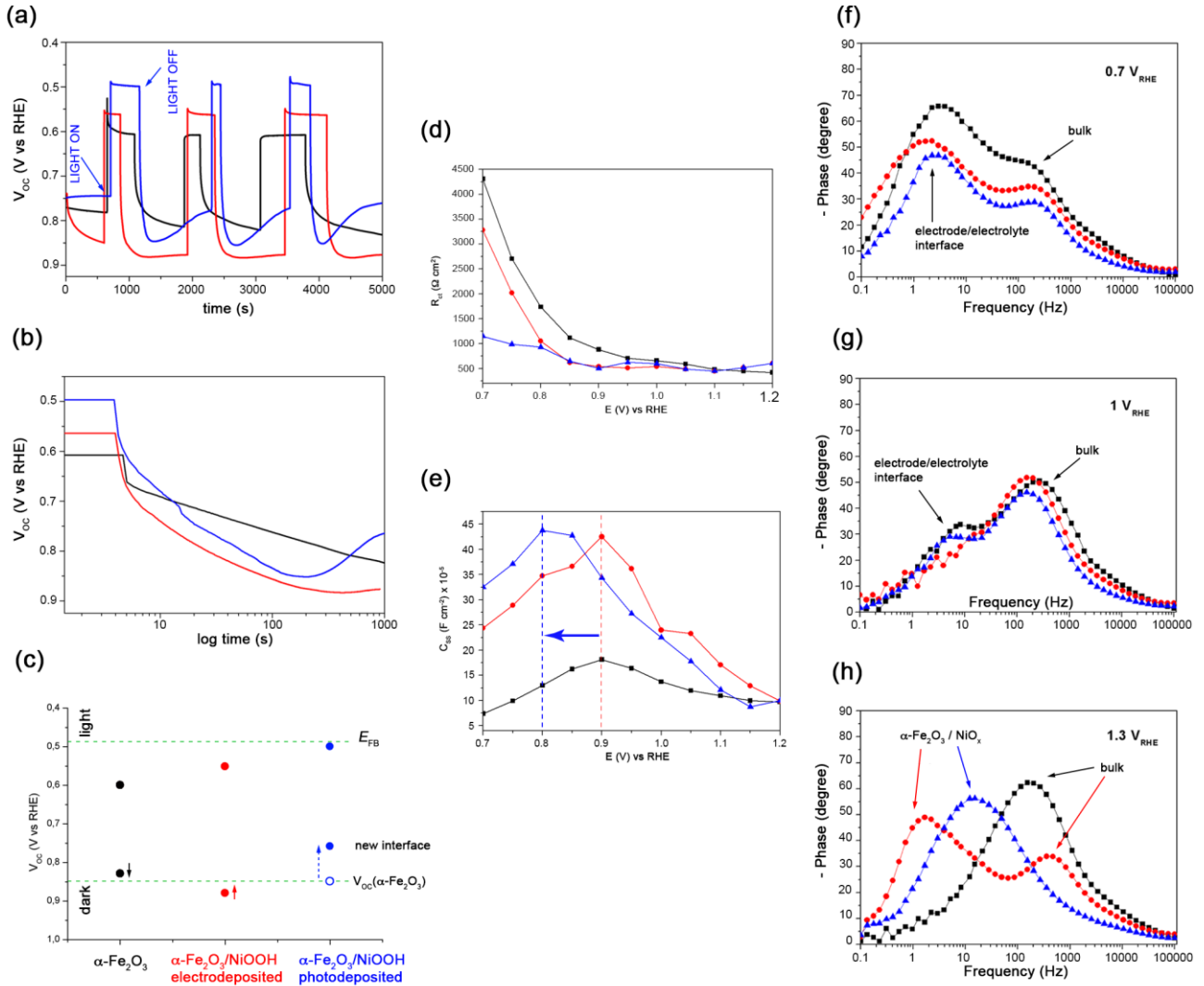
Figure 5. a) V_{OC} decay plot and b) V_{OC} decay log plot of bare α-Fe$_2$O$_3$, α-Fe$_2$O$_3$/NiOx electrodeposited, and α-Fe$_2$O$_3$/NiOx photodeposited. c) Summary of V_{OC} values of the hematite electrodes before and after NiOx deposition in light and dark conditions. The arrows indicate the values to which the electrodes are stabilized. Different deposition techniques bring the V_{OC} in light to approach at α-Fe$_2$O$_3$ flat band potential thanks to the passivation of superficial defects. Also, a new energetic level in the V_{OC} in light is established for α-Fe$_2$O$_3$/NiO$_x$ photodeposited. d) Plot of charge transfer resistance (R_{ct}) and e) surface state capacitances (C_{ss}) at electrode/electrolyte interface versus potential. f-h) Bode plots of bare α-Fe$_2$O$_3$, α-Fe$_2$O$_3$/NiOx electrodeposited and α-Fe$_2$O$_3$/NiOx photodeposited electrodes at 0.7 V (f), 1 V (g) and 1.3 V (h). In all plots colour legend corresponds to bare α-Fe$_2$O$_3$ (black line), α-Fe$_2$O$_3$/NiOx electrodeposited (red line), and α-Fe$_2$O$_3$/NiOx photodeposited (blue line) electrodes.

Electrodeposition is based on the migration of ions in the electrolyte (i.e., OH$^-$ and Ni^{2+}) and the quality of the deposit depends on α-Fe$_2$O$_3$ roughness at the surface. An intricate network of grains

15

with dimension on the order of 75-100 nm forms our α-Fe$_2$O$_3$. Therefore, during NiO$_x$ deposition will exist area of the electrode that would experience different resistance and current flow at the nanoscale. The direct outcome is the creation of a discontinuous NiO$_x$ layer that produces only a partial (and random) passivation of surface defects resulting in a modest V_{OC} in light shift (40 mV, see Figure 5c) and in the same Fermi level in dark as for α-Fe$_2$O$_3$.

Differently, during NiO$_x$ photodeposition at open circuit voltage α-Fe$_2$O$_3$ surface defects preferentially trap photogenerated charges[40] that subsequently oxidize Ni^{2+} to Ni^{3+} and favour the nucleation of NiO$_x$ overlayer. The NiO$_x$ growth is homogeneous and conformal to the α-Fe$_2$O$_3$ scaffold because not only the defects but also all Fe-O atomic sites at the surface are activated. This straightforward deposition method allows the complete passivation of surface defects and produces a photoanode with V_{OC} approaching the flat band potential limit (0.48 V, see Figure 5c).[12]

We have shown how surface defects regulate the Fermi level in light and in dark conditions. With NiO$_x$ photodeposition we modify the majority of these defective sites and thus it is expected that Fermi level pinning would not affect anymore the band bending. This argument might justify the cathodic shift of V_{ON} observed for α-Fe$_2$O$_3$/NiO$_x$ photodeposited with respect to α-Fe$_2$O$_3$ and α-Fe$_2$O$_3$/NiO$_x$ electrodeposited. However, if the V_{ON} shift would be regulated only by surface energetics, the photovoltage change ($V_{ph} = V_{OC\ light} - V_{OC\ dark}$) among the photoanodes would correspond to the V_{ON} shift.[12,24] Importantly, V_{ph} is similar for α-Fe$_2$O$_3$, α-Fe$_2$O$_3$/NiO$_x$ electrodeposited, and α-Fe$_2$O$_3$/NiO$_x$ photodeposited and calculated values are 240 mV, 280 mV, and 250 mV.

Therefore, it is necessary to consider also the kinetic aspects that may influence the *J-V* curve. As described in equation *(2)* the concentration of surface holes are strictly related to the water oxidation overpotential, that in turn it is intimately regulated by the charge transfer kinetics at the electrode/electrolyte interface.

To justify the improvement in performance in kinetics terms after NiO$_x$ deposition on the α-Fe$_2$O$_3$ electrodes electrochemical impedance spectroscopy (EIS) measurements are carried out.

Figure 5d reports the trend of R_{ct} (charge transfer resistance) and C_{ss} (surface states capacitance) at electrode/electrolyte interface varying the applied bias. The data are fitted by using the equivalent circuit proposed by Klahr.[23]

At low potentials (i.e., 0.7 V), R_{ct} decreases of 18% from pure α-Fe$_2$O$_3$ (R_{ct} = 4300 Ω*cm^2) to α-Fe$_2$O$_3$/NiO$_x$ electrodeposited (R_{ct} = 3500 Ω*cm^2). Differently, the R_{ct} of α-Fe$_2$O$_3$/NiO$_x$ photodeposited electrode is drastically reduced by 4 times. This difference between the R_{ct} of the samples can justify the cathodic shift of V_{ON}. Moving towards anodic potentials, R_{ct} values tend to conform since charge transfer to the electrolyte is not anymore the limiting process.[41]

C_{ss} of bare α-Fe$_2$O$_3$ is included between $0.5*10^{-4}$ and $1.5*10^{-4}$ F cm^{-2}, with the maximum positioned at 0.9 V. After NiO$_x$ deposition, the capacitance is boosted of about 3 times. Both the deposition techniques produce the same C_{ss} increase that can be ascribed to the passivation of surface states and to the high ion permeability of NiO$_x$ structures.[19,27,42] On the contrary, C_{ss} peak for the α-Fe$_2$O$_3$/NiO$_x$ photodeposited is cathodically shifted by 100 mV with respect to both α-Fe$_2$O$_3$ and α-Fe$_2$O$_3$/NiO$_x$ electrodeposited. This shift is strictly related to the cathodic shift of V_{ON} and highlights the importance of the linking formed between NiO$_x$ and α-Fe$_2$O$_3$, which for NiO$_x$ photodeposited facilitates the charge transfer at the electrode/electrolyte interface

No variations were observed in the values of R_{bulk} (bulk resistance) and C_{bulk} (bulk capacitance) after either NiO$_x$ electro- or photodeposition (Figure S7 and S8), in agreement with previous report.[19]

Additional kinetics considerations can be deducted from the Bode plots. Figure 5 shows the Bode plots of α-Fe$_2$O$_3$, α-Fe$_2$O$_3$/NiO$_x$ electrodeposited, and α-Fe$_2$O$_3$/NiO$_x$ photodeposited at three representative applied potentials. At 0.7 V and 1 V all photoanodes have a similar behaviour and show two characteristic peaks: the first one at 5 Hz is typical of the electrode/electrolyte interface; the second one at 152 Hz is typical of the bulk feature. At 0.7 V, the peak at 5 Hz is predominant and can be associated to the charges locked at interface.[19] At 1 V, the peak at 152 Hz prevails, indicating

that the limiting factor in the charge transfer is relative to the conducting properties of the bulk α-Fe_2O_3. At 1.3 V, the trend of the curves changes. The bare electrode shows only one peak (150 Hz) associated to the behaviour of the bulk α-Fe_2O_3. Differently, α-Fe_2O_3/NiO_x electrodeposited shows two peaks: one at 300 Hz, that can be associated to the bulk α-Fe_2O_3, and another at 2 Hz, associated to the charge transfer at the α-Fe_2O_3/NiO_x interface. α-Fe_2O_3/NiO_x photodeposited electrode shows again only one peak but at about 12 Hz relative to α-Fe_2O_3/NiO_x interface. The higher frequency with respect to the NiO_x electrodeposited photoanode suggests a higher transfer rate between α-Fe_2O_3 and NiOx photodeposited. It is also worth noting that α-Fe_2O_3/NiO_x electrodeposited shows two peaks also at 1.3 V, while α-Fe_2O_3/NiO_x photodeposited is characterized by only one capacitive process. This proofs that in the first case the α-Fe_2O_3 "see" the electrolyte and regulates the energetics of the electrode through defects (V_{OC} in the dark is the same with respect to the bare α-Fe_2O_3), while when NiO_x is photodeposited a new high performing interface is created and α-Fe_2O_3 is buried by the overlayer.

Finally, during current generation the photogenerated holes migrate across the electrode/electrolyte interface and sustain the water oxidation reaction. For α-Fe_2O_3/NiO_x electrodes, holes hop from α-Fe_2O_3 to NiO_x, changing the nickel oxidation state. If the surface of one electrode would be partially covered with NiO_x (i.e., NiO_x electrodeposited) some holes would travel from α-Fe_2O_3 to the electrolyte, while the remainders oxidize Ni. Otherwise, if the surface of α-Fe_2O_3 would be completely and homogeneously covered with the overlayer (i.e., NiO_x photodeposited), before reaching the electrolyte more holes would oxidize the NiO_x. In order to test this hypothesis, we compare the area of Ni oxidation waves observed during CV scan in dark and light conditions. The Ni^{2+}/Ni^{3+} oxidation peak in dark condition of α-Fe_2O_3/NiO_x electrodeposited is 3 times higher than the same in light condition. This means that in light condition a big part of the NiO_x is already oxidized by the photo-holes produced within α-Fe_2O_3. In α-Fe_2O_3/NiO_x photodeposited this effect is even more emphasized and the area is almost 6 times lower. As a matter a fact, this is a further confirmation that through NiO_x photodeposition we create a more conformal overlayer than that produced by

electrodeposition. Only the α-Fe$_2$O$_3$/NiO$_x$ photodeposited photoanode behaves as unique materials that show a renewed interface with higher charge transfer capabilities.

3. Conclusion

In summary, the photocurrent onset potential of α-Fe$_2$O$_3$ photoanodes is controlled by the surface energetic and kinetics at the electrode/electrolyte interface through few atomic layers of NiO$_x$. Electrodeposited NiO$_x$ coating produces an increase of current density at high bias, while photodeposition NiO$_x$ induces both an increase of current density and a 200 mV cathodic shift of the onset potential, which reaches 0.58-0-6 V. This is due to the different α-Fe$_2$O$_3$/NiO$_x$ established junction and not to the electrocatalytic activity of the deposited layers. Both electrodeposition and photodeposition of NiO$_x$ on α-Fe$_2$O$_3$ produces thin amorphous overlayers few nm in thickness. Electrodeposition produces a NiO$_x$ film uneven at the nanoscale, while NiO$_x$ photodeposition is based on the light-activation of all surface atoms, which act as nucleation centers for the growth of a homogeneous and conformal overlayer. Only this latter is able to produce a quenching of the electron-hole recombination, which is responsible of the cathodic shift of V_{on}. This is possible because NiO$_x$ electrodeposited induces only a partial passivation of surface defects, while the NiO$_x$ photodeposition is able to completely modify the α-Fe$_2$O$_3$ defective sites. This is clearly shown through open circuit voltage measurements. The quasi-Fermi level in light of α-Fe$_2$O$_3$ (0.61 V) was negatively shifted of 40 mV once NiO$_x$ electrodeposition is applied, while a 110 mV shift is seen for the NiO$_x$ photodeposited electrodes that make V_{OC} approaching the flat band potential. The Fermi level in dark, instead, reveals that only when α-Fe$_2$O$_3$ surface is completely buried from water (i.e., NiO$_x$ photodeposited) a new surface energetics is created. The direct consequence is that α-Fe$_2$O$_3$/NiO$_x$ behaves as a new material with improved charge transfer kinetics at the electrode/electrolyte interface.

Therefore, both the complete surface defects passivation and a better charge transfer across the photoelectrode/electrolyte interface are the reason why the onset potential is cathodically shifted

only in the case of α-Fe$_2$O$_3$/NiO$_x$ photodeposited. These findings can be extended to any oxide semiconductor used in the anodic water splitting half reaction.

This study highlights the importance of the semiconductor/catalyst interface in defining the PEC performance. We have also shown how surface energetic and kinetics are strictly correlated and that the tuning of the former (i.e., different degree of surface defects passivation) may produces enormous change on the latter.

We have unravelled the reasons underlying the cathodic shift in onset potential that often is observed when photoanodes are functionalized with overlayers setting a new level of understanding in the run toward low-bias photoanodes for solar water splitting.

4. Experimental section

Hematite films growth. Thin films of hematite were deposited on fluorine-doped tin oxide (FTO)-coated glass substrates (Solaronix, 10 Ω/sq.) by thermal-solution deposition at 70°C for 3 h using as precursors Fe$_2$Cl$_3$·6H$_2$O (0.15M) and NaNO$_3$ (1M) in water solution, at pH 1.5 optimized with HCl solution.[2] The samples were calcined at 550°C for 1h, followed by 20 min at 800°C.[43]

NiO$_x$ deposition. NiO$_x$ catalyst films were deposited onto hematite electrodes both by electro- and photo- deposition.[19] α-Fe$_2$O$_3$ electrodes were immersed in a solution containing 0.1 M Ni(NO$_3$)$_2$·6H$_2$O, whose pH was corrected with NaOH until pH 6.6. Before use the solution was treated in nitrogen for 1h. The electrodeposition of NiO$_x$ was carried out in dark at 1.23V vs RHE for 60s, 600s, 1200s and 1800s. Photodeposition was carried out at V$_{oc}$ vs Ag/AgCl. The thickness of the NiO$_x$ layer was controlled by varying the photodeposition times. For the electrodes reported herein, 4 different deposition times were used: 60s, 300s, 600s and 1200s. After catalyst deposition, the electrodes were lightly rinsed with DI water to remove any excess Ni ions.

Characterizations. X-ray diffraction (XRD) measurement was performed at room temperature in the $20° \leq 2\theta \leq 70°$ range employing the Cu-Kα radiation at room temperature. Diffraction data were collected by placing directly the FTO films within the sample holder of the diffractometer. SEM

images of cross-section were collected by a XL30 Environmental Scanning Electron Microscopy (ESEM FEG Philips) at 20 kV under low vacuum (0.8 torr) condition. TEM and HRTEM micrographs were collected by a ZEISS LIBRA200FE. Electron Spectroscopic Imaging (ESI) and elemental distribution maps for Fe and Ni were collected via energy-filtering electrons at related L_3 edges of electron energy loss (EEL). The ZEISS in-column Omega filter spectrometer was used next to the Olympus-SIS iTEM software for data collection and analysis. XPS was performed with a M-Probe—SSI instrument equipped with a monochromatic Al Kα source (1486.6 eV) with a spot size of 200 x 750 mm and a pass energy of 25 eV, providing a resolution for 0.74 eV.

CL spectroscopy was carried out with a commercial Gatan MonoCL2 system, fitted onto an S360 Cambridge SEM. The system is equipped with a 1800 lines/mm grating and a multi-alkali photomultiplier sensitive in the range 350 – 830 nm (3.6 eV - 1.5 eV). The CL spectra were collected at room temperature with an accelerating voltage of 10 keV, a beam current of 50 nA, and a spectral resolution of 9 nm (about 70 meV). The single peak parameters are, thus, evaluated by a deconvolution procedure using a standard Levenberg-Marquardt algorithm for the minimization of the Chi Square. In order to avoid any possible artifacts the fitting parameters peak position (x_C) and amplitude (A) were left free, while constraints were applied to the full width half maximum (w). We impose a w maximum equal to 0.5 eV. At the end all the peak position are affected by an error of 0.01 eV, that is less than the error due to the spectral resolution of the measurement. The amplitude and the full width half maximum have a relative error of the 5%.

Electrochemical measurements. The electrodes were electrochemically characterized in a three electrodes system: the RE (reference electrode) was a silver chloride electrode (Ag/AgCl/Sat. KCl), while a high surface area Pt mesh was the CE. The potential (E) was referred to the reversible hydrogen electrode (RHE) scaled through the Nernst equation:

$$E_{RHE} = E_{AgCl} + 0.197\,\text{V} + 0.059\,p\text{H}$$

where E_{AgCl} is the measured electrode potential vs. the used reference electrode and 0.197 is the reference electrode standard potential vs. the normal hydrogen electrode. In the manuscript, all

measurements are reported with respect to RHE. The measurements were carried out in 1 M NaOH aqueous solution at pH 13.6. Cyclic Voltammetry (CV) curves were measured at a scan rate of 10 mV/s. PEC measurements were made with a PGSTAT204 Autolab potentiostat. Electrochemical Impedance Spectroscopy (EIS) and data were gathered using a 10 mV amplitude perturbation at frequency between 0.01 Hz and 1 MHz. 300 W xenon arc lamp (calibrated at 100 mW/cm^2) coupled to an AM 1.5 G filter was used as light source. At least three electrodes of each type were fabricated and tested. All electrodes showed similar characteristics and representative data are reported.

[1]   S. C. Warren, K. Voïtchovsky, H. Dotan, C. M. Leroy, M. Cornuz, F. Stellacci, C. Hébert, A. Rothschild, M. Grätzel, *Nat. Mater.* **2013**, *12*, 842.

[2]   J. Y. Kim, G. Magesh, D. H. Youn, J. Jang, J. Kubota, K. Domen, J. S. Lee, *Sci. Rep.* **2013**, *3*, 2681.

[3]   O. Zandi, T. W. Hamann, *Phys. Chem. Chem. Phys.* **2015**, *17*, 22485.

[4]   I. S. Cho, H. S. Han, M. Logar, J. Park, X. Zheng, *Adv. Energy Mater.* **2015**, DOI: 10.1002/aenm.201501840.

[5]   Y. Ling, G. Wang, D. A. Wheeler, J. Z. Zhang, Y. Li, *Nano Lett.* **2011**, *11*, 2119.

[6]   Y. Ling, G. Wang, J. Reddy, C. Wang, J. Z. Zhang, Y. Li, *Angew. Chemie Int. Ed.* **2012**, *51*, 4074.

[7]   L. Li, Y. Yu, F. Meng, Y. Tan, R. J. Hamers, S. Jin, *Nano Lett.* **2012**, *12*, 724.

[8]   C. Lee, L. Wang, Y. Kado, M. S. Killian, P. Schmuki, *ChemSusChem* **2014**, *7*, 934.

[9]   M. Marelli, A. Naldoni, A. Minguzzi, M. Allieta, T. Virgili, G. Scavia, S. Recchia, R. Psaro, V. Dal Santo, *ACS Appl Mater Interfaces* **2014**, *6*, 11997.

[10] C. Sci, F. Le Formal, T. Nicolas, M. Cornuz, T. Moehl, M. Gr, K. Sivula, *Chem. Sci.* **2011**, *2*, 737.

[11] L. Steier, I. Herraiz-cardona, S. Gimenez, F. Fabregat-santiago, J. Bisquert, S. D. Tilley, M. Grätzel, *Adv. Funct. Mater.* **2014**, *24*, 7681.

[12] J.-W. Jang, C. Du, Y. Ye, Y. Lin, X. Yao, J. Thorne, E. Liu, G. McMahon, J. Zhu, A. Javey, J. Guo, D. Wang, *Nat. Commun.* **2015**, *6*, 7447.

[13] M. S. Prévot, K. Sivula, *J. Phys. Chem. C* **2013**, *117*, 17879.

[14] K. Sivula, B. Florian, L. Formal, M. Gra, *Adv. Funct. Mater.* **2010**, *20*, 1099.

[15] T. Hisatomi, H. Dotan, M. Stefi, K. Sivula, A. Rothschild, *Adv. Mater.* **2012**, *24*, 2699.

[16] K. J. Mcdonald, K. Choi, *Chem. Mater.* **2011**, *23*, 1686.

[17] E. Environ, D. K. Zhong, M. Cornuz, K. Sivula, M. Gr, D. R. Gamelin, *Energy Environ. Sci.* **2011**, *4*, 1759.

[18] S. O. Material, N. York, A. Nw, *Science* **2014**, *343*, 990.

[19] F. Malara, A. Minguzzi, M. Marelli, S. Morandi, R. Psaro, V. Dal Santo, A. Naldoni, *ACS Catal.* **2015**, *5*, 5292.

[20] S. D. Tilley, M. Cornuz, K. Sivula, M. Grätzel, *Angew. Chem. Int. Ed.* **2010**, *49*, 6405.

[21] E. Environ, T. Nicolas, K. Sivula, M. Gr, *Energy Environ. Sci.* **2011**, *4*, 2512.

[22] O. Zandi, T. W. Hamann, *J. Phys. Chem. Lett.* **2014**, *5*, 1522.

[23] B. Klahr, S. Gimenez, F. Fabregat-santiago, T. Hamann, J. Bisquert, *J. Am. Chem. Soc.* **2012**, *134*, 4294.

[24] J. E. Thorne, S. Li, C. Du, G. Qin, D. Wang, *J. Phys. Chem. Lett.* **2015**, *6*, 4083.

[25] M. Gao, W. Sheng, Z. Zhuang, Q. Fang, S. Gu, J. Jiang, Y. Yan, *J. Am. Chem. Soc.* **2014**, *136*, 7077.

[26] Y. Li, A. Selloni, *ACS Catal.* **2014**, *4*, 1148.

[27] R. L. Doyle, I. J. Godwin, M. P. Brandon, M. E. G. Lyons, *Phys. Chem. Chem. Phys.* **2013**, 13737.

[28] R. L. Doyle, M. E. G. Lyons, *Phys. Chem. Chem. Phys.* **2013**, *15*, 5224.

[29] N. Ii, H. Bode, K. D. J. Witte, *Electrochim. Acta* **1966**, *11*, 1079.

[30] V. A. Online, G. Wang, Y. Ling, X. Lu, T. Zhai, F. Qian, Y. Tong, Y. Li, *Nanoscale* **2013**, *5*, 4129.

[31] A. Naldoni, C. L. Bianchi, C. Pirola, K. S. Suslick, *Ultrason. Sonochem.* **2013**, *20*, 445.

[32] B. M. Klahr, T. W. Hamann, *J. Phys. Chem. C* **2011**, *115*, 8393.

[33] M. F. Chioncel, J. Piqueras, *J. Appl. Phys.* **2008**, *104*, 124311.

[34] E. Environr, D. A. Wheeler, G. Wang, Y. Ling, Y. Li, J. Z. Zhang, *Energy Environ. Sci.* **2012**, *5*, 6682.

[35] N. J. Cherepy, D. B. Liston, J. A. Lovejoy, H. Deng, J. Z. Zhang, *J. Phys. Chem. B* **1998**, *102*, 770.

[36] Q. Dai, M. E. Foley, C. J. Breshike, A. Lita, F. Strouse, *J. Am. Chem. Soc.* **2011**, *133*, 15475.

[37] M. G. Walter, E. L. Warren, J. R. McKone, S. W. Boettcher, Q. Mi, E. a. Santori, N. S. Lewis, *Chem. Rev.* **2010**, *110*, 6446.

[38] L. S. Parenr, A. J. Bard, A. B. Bocarsly, F. F. Fan, E. G. Walton, M. S. Wrighton, *J. Am. Chem. Soc.* **1980**, *102*, 3671.

[39] M. Barroso, A. J. Pendlebury, Stephanie R. Cowan, J. R. Durrant, **2013**, *4*, 2724.

[40] L. Amidani, A. Naldoni, M. Malvestuto, M. Marelli, P. Glatzel, V. Dal Santo, F. Boscherini, *Angew. Chemie Int. Ed.* **2015**, *54*, 5413.

[41] K. Sivula, *J. Phys. Chem. Lett.* **2013**, *4*, 1624.

[42] K. M. H. Young, T. W. Hamann, *Chem. Commun.* **2014**, *3*, 8727.

[43] K. Sivula, R. Zboril, F. Le Formal, R. Robert, A. Weidenkaff, J. Tucek, J. Frydrych, M. Gra, *J. Am. Chem. Soc.* **2010**, 7436.